Available online at www.sciencedirect.com
ScienceDirect
International Journal of Heat and Mass Transfer 51 (2008) 1505–1515
International Journal of HEAT and MASS TRANSFER
www.elsevier.com/locate/ijhmt

Near-infrared light heating of a slab by embedded nanoparticles

Indra K. Tjahjono, Yildiz Bayazitoglu *

Department of Mechanical Engineering and Materials Science, Rice University, Houston, TX 77005, United States

Received 15 January 2007; received in revised form 24 July 2007
Available online 31 October 2007

Abstract

Exposed to spectral and uniform light, the heating of a one-dimensional, conducting and radiatively participating medium due to embedded absorbing and scattering nanoparticles is solved. Spherical harmonics approximation is used to solve the radiative transfer equation and the finite difference explicit method is used to find the temperature distribution in a generic slab having both boundaries subjected to convection. The host medium is transparent to spectral radiation and the temperature distribution is obtained when the temperature of the irradiated boundary reaches a desired point specified to ensure that any temperature in the medium does not exceed its melting temperature. It is found that the variation of the concentration and configuration of the embedded nanoparticles, particularly gold nanoshells, changes the radiative transfer spectrum, which leads to an alteration in the local heat generation spectrum and the resulting temperature distribution in the medium. It is shown that a gold nanoshell configuration with a great amount of scattering increases the internal diffuse radiation, which creates a more even radiative distribution, while a configuration with a great amount of absorption promotes a high amount of absorption in the entry region and very little in the rear region, leading to the formation of a large temperature gradient between the two boundaries. The present study provides a framework from which the photothermal heating of nanoparticle mixtures in non-transparent host media may be applied.

Keywords: Light heating; Infrared; Nanoparticles; Nanoshells; Heat transfer

1. Introduction

In the last few years, study on radiation induced by microscale or nanoscale particles has started to catch several researchers' attention; however, minimal attention has been directed to gold nanoshells. Gold nanoshells are a new type of nanoparticle that consists of a dielectric silica core wrapped with a thin gold shell. Nanoshells have optical resonances with tunable wavelengths across the visible and the near-infrared regime. Their wavelength tunability is achieved by changing the relative dimensions of the silica core and the gold shell [1,17]. When a collection of gold nanoshells is embedded and distributed inside a medium that is transparent in the near-infrared wavelength spectrum, the gold-nanoshell-embedded medium will act as a semitransparent medium. When subjected to light at near-infrared wavelengths, not only will the nanoshells attenuate incident radiation due to absorption and scattering, they will also generate internal heating inside the medium. Doing so, media can be represented as particle fields, and radiation effects can be modeled.

Analysis of radiation effects in these kinds of media has been studied in the past [18] and also recently [19,20]. A theoretical study of the radiation effect in heating and melting of a fused silica spherical particle was done to observe the melting behavior in detail up to the particulate level [19]. Fused silica was chosen because it acts as a semitransparent medium and allows internal radiation, i.e. internal absorption and emission. It also has a high and unique melting temperature, and its properties are easily available in the literature. Unfortunately, this theoretical study did not provide information about its heat generating profile when fused silica particles are spread inside a medium. The other models of ray tracing for radiative heat transfer problems where the participating medium is represented by

* Corresponding author. Tel.: +1 713 8380979.
E-mail address: bayaz@rice.edu (Y. Bayazitoglu).

0017-9310/$ - see front matter © 2007 Elsevier Ltd. All rights reserved.
doi:10.1016/j.ijheatmasstransfer.2007.07.047

Nomenclature

Symbols

a	total radius of nanoshells, m or nm
B's	analytical constants
C's	analytical constants
c	specific heat, J/kg K
E_b	blackbody emissive power, W/m^2
G	irradiance, W/m^2
H	internal irradiation to surface boundaries
h	convective heat transfer coefficient, W/m^2 K
I	intensity of radiation
I_b	blackbody intensity of radiation
k	thermal conductivity, W/m K
$\hat{\mathbf{k}}$	unit direction along z-axis
L	length of slab
M	number of nodes
m	node
N_T	number of particles per unit volume or particle concentration, particles/m^3
n	index of refraction
Q	efficiency
q''	heat flux, W/m^2
S	source function
$\hat{\mathbf{s}}$	arbitrary direction of propagation
$\hat{\mathbf{s}}_c$	direction of propagation of collimated radiation in the medium
$\hat{\mathbf{s}}_i$	direction of propagation of input radiation before entering the medium
T	temperature, °C or K
T^P	temperature at time P, °C or K
t	time, s
Δt	time increment, s
U^*	normalized heat generation
u'''	heat generation, W/m^3
z	axis of coordinate system pointing towards the depth normal to boundary, m
Δz	spatial increment, m

Greek symbols

α	thermal diffusivity, m^2/s
β	extinction coefficient, m^{-1}
Φ	normalized irradiance
Φ_b	normalized blackbody emissive term
κ	absorption coefficient, m^{-1}
μ	$\cos\theta$
μ_c	$\cos\theta_c$
Ω	solid angle
θ	angle between arbitrary direction of propagation $\hat{\mathbf{s}}$ and $\hat{\mathbf{k}}$
θ_c	angle between direction of propagation of collimated radiation $\hat{\mathbf{s}}_c$ and $\hat{\mathbf{k}}$
ρ	density, kg/m^3
ρ	reflectivity
σ_s	scattering coefficient, m^{-1}
τ	optical depth or optical location
τ_L	optical length
ω	scattering albedo
ξ_1	analytical constant
Ψ	normalized radiative heat flux

Subscripts

c	correspond to collimated radiation
d	correspond to diffuse radiation
i	correspond to medium outside the slab medium
in	correspond to input
m	correspond to node
md	correspond to host medium
R	correspond to total radiation, summation of diffuse and collimated radiation
∞	correspond to surrounding

Greek subscripts

β	correspond to extinction
κ	correspond to absorption
λ	spectral
σ_s	correspond to scattering

particles did not explain any heat production by particles [20]. The only reports on gold nanoshell-assisted heat generation in a solid medium are found in recent works. The reports describe a photothermally responsive nanoshell–polymer composite that shrinks when heated up [21,22]. It is manufactured for the potential purpose of modulated drug delivery. However, the lack of radiative heat transfer analysis has motivated the authors to study the participating embedded medium created by gold nanoshells.

The objective of this study is to provide a one-dimensional radiative heat transfer analysis of a participating slab medium heating due to the existence of gold nanoshells. A first-order spherical harmonics approximation [23] is employed to solve the radiative heat transfer of the slab being subjected to spectral irradiation from an external source at a near-infrared wavelength. The radiative transfer is then combined with thermal energy to observe the heat generation and temperature distribution of the medium at any given time.

2. Radiative transfer analysis

A semitransparent medium is engineered by embedding gold nanoshells in a transparent slab. Light at selected

wavelength λ is aimed to a single face of the slab uniformly at an angle θ_i from normal. To ease further explanation, the slab's face where the light enters the medium is called the entry boundary ($z = 0, \tau_\lambda = 0$), the one where the light leaves the medium is called the exit boundary ($z = L, \tau_\lambda = \tau_{L\lambda}$), and the region in between can be divided into two parts: entry region ($0 < z < 0.5L$, $0 < \tau_\lambda < 0.5\tau_{L\lambda}$) and rear region ($0.5L < z < L$, $0.5\tau_{L\lambda} < \tau_\lambda < \tau_{L\lambda}$). Without the gold nanoshell embedment, the slab is considered transparent to spectral irradiation, meaning the penetrating light experiences negligible attenuation by the slab medium. The semitransparent medium is defined as a gold-nanoshell-embedded medium that is capable of attenuating a penetrating light's intensity at the input wavelength.

The radiative transfer equation [23] of a propagating light inside an absorbing and isotropically scattering, one-dimensional plane parallel medium with constant radiative properties is given as

$$\mu \frac{\mathrm{d}I_{\mathrm{R}\lambda}(\tau_\lambda, \hat{\mathbf{s}})}{\mathrm{d}\tau_\lambda} + I_{\mathrm{R}\lambda}(\tau_\lambda, \hat{\mathbf{s}}) = S(\tau_\lambda, \hat{\mathbf{s}}) \tag{1}$$

where $S(\tau_\lambda, \hat{\mathbf{s}})$ is the source function defined as

$$S(\tau_\lambda, \hat{\mathbf{s}}) = \frac{\omega_\lambda}{4\pi} \int_{4\pi} I_{\mathrm{R}\lambda}(\tau_\lambda, \hat{\mathbf{s}}) \mathrm{d}\Omega \tag{2}$$

$I_{\mathrm{R}\lambda}(\tau_\lambda, \hat{\mathbf{s}})$ is the spectral intensity of radiation at optical location τ_λ in the medium propagating towards an arbitrary direction $\hat{\mathbf{s}}$, which is characterized by the term $\mu = \hat{\mathbf{s}} \cdot \hat{\mathbf{k}} = \cos\theta$. As illustrated in Fig. 1, direction $\hat{\mathbf{s}}_\mathrm{c}$ is refracted from direction $\hat{\mathbf{s}}_\mathrm{i}$ due to a mismatch of refractive indices. The angle θ_c defines the angle between the direction of propagation of collimated radiation and $\hat{\mathbf{k}}$ direction. The subscript λ denotes the spectral characteristic, i.e. obeying the optical properties at selected wavelength. The refraction and reflection phenomena at the boundaries due to refractive index mismatch obey the Snell's Law and Fresnel reflection, respectively [23]. Assumptions taken in the radiative transfer analysis are: (1) emission from the medium and nanoshells is negligible, (2) the host medium is homogeneous, (3) the gold nanoshells in the medium are distributed evenly, (4) all of the nanoshells in the medium have the same size and aspect ratio (core diameter/shell diameter), and (5) the host medium is transparent to spectral irradiation.

The spectral absorption and scattering coefficients, κ_λ and $\sigma_{\mathrm{s}\lambda}$, respectively are deduced from the spectral absorption and scattering efficiencies of the nanoshells, $Q_{\kappa\lambda}$ and $Q_{\sigma_\mathrm{s}\lambda}$, respectively under the following relations:

$$\kappa_\lambda = \pi a^2 Q_{\kappa\lambda} N_T \tag{3}$$

$$\sigma_{\mathrm{s}\lambda} = \pi a^2 Q_{\sigma_\mathrm{s}\lambda} N_T \tag{4}$$

where N_T is the number of nanoshells per unit volume. The absorption or scattering coefficient defines how much absorption or scattering, respectively, is performed to the incoming light per unit depth at a particular wavelength. The total spectral extinction efficiency, $Q_{\beta\lambda}$, is equal to summation of spectral absorption and scattering efficiencies from each of the nanoshells. Also, the summation of the spectral absorption and scattering coefficients of the nanoshells will be the total spectral extinction coefficient, β_λ. In order to observe the proportion of absorption and scattering to total extinction, the spectral scattering albedo, ω_λ, is introduced to define the ratio of the spectral scattering coefficient to spectral extinction coefficient, i.e. $\sigma_{\mathrm{s}\lambda}/\beta_\lambda$. The term τ_λ denotes the optical location in the medium measured from the entry boundary in the $\hat{\mathbf{k}}$ direction. It is obtained by multiplying the extinction coefficient, β_λ, with z. Thus, the optical length, $\tau_{L\lambda}$, is equal to $\beta_\lambda L$.

At the entry boundary, the input irradiation is divided into two parts: the first is where the light is slightly outside the medium at a negligible distance from the boundary, i.e. before entering the boundary, $I_{\mathrm{in},\lambda}(0^-)$, and the second is where the light is slightly inside the medium at a negligible distance from the boundary, $I_{\mathrm{in},\lambda}(0^+)$. They are described as follows:

$$I_{\mathrm{in},\lambda}(0^-, \hat{\mathbf{s}}) = q''_{\mathrm{in},\lambda} \delta(\hat{\mathbf{s}} - \hat{\mathbf{s}}_\mathrm{i}) \tag{5}$$

$$I_{\mathrm{in},\lambda}(0^+, \hat{\mathbf{s}}) = (1 - \rho_\lambda(0)) q''_{\mathrm{in},\lambda} \delta(\hat{\mathbf{s}} - \hat{\mathbf{s}}_\mathrm{c}) \tag{6}$$

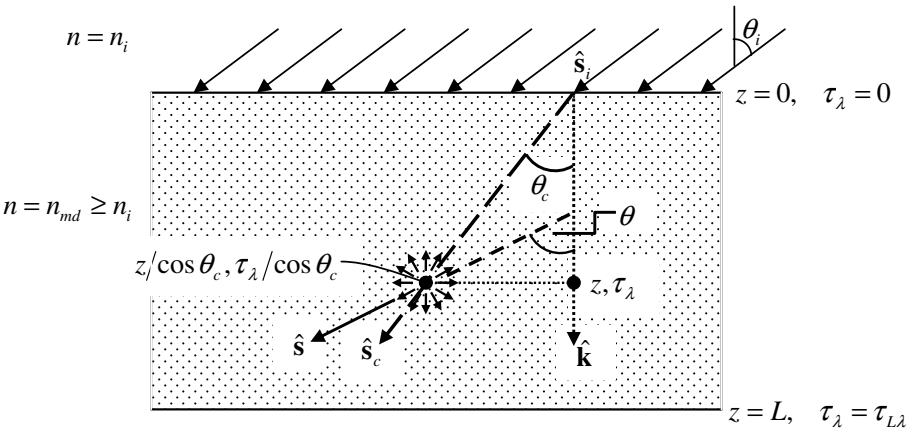

Fig. 1. Schematic of light propagation in the slab.

The input irradiation should be at the particular wavelength such that its intensity attenuates due to interaction with gold nanoshells, normally in the near-infrared regime. In the present work, the light attenuation due to absorption or scattering by the medium is ignored because the medium is assumed to be transparent with respect to the input wavelength.

As propagating light is absorbed and scattered by nanoshells, the intensity of radiation can be divided into two components. The first component is called the collimated intensity of radiation, $I_{c\lambda}$, which is the intensity of radiation that decays along the depth. The second component is called the diffuse intensity of radiation, $I_{d\lambda}$, which is the intensity of radiation due to scattering and emission from nanoshells. However, in the present work, emission is neglected. Thus, the intensity of radiation in the left hand side of Eq. (1) at location τ_λ in the medium propagating towards an arbitrary direction $\hat{\mathbf{s}}$ can be described as follows:

$$I_{R\lambda}(\tau_\lambda,\hat{\mathbf{s}}) = I_{c\lambda}(\tau_\lambda,\hat{\mathbf{s}}) + I_{d\lambda}(\tau_\lambda,\hat{\mathbf{s}}) \tag{7}$$

When light encounters a nanoshell, it can be reflected, refracted, or diffracted specularly or diffusely. Collimated light that does not reflect off the entry boundary layer enters the medium with a factor of $(1-\rho_\lambda(0))$. Along the depth of the medium, multiple interactions of the nanoshells with the impending collimated rays exponentially attenuates the intensity of the collimated light. However, that light which is not scattered or absorbed continues to travel along the depth of the medium, albeit with decreasing intensity, allowing the remnant of collimated rays to contribute to the collimated source function. Those specular reflections from numerous gold nanoshells in the medium pointing in the same direction as the collimated radiation also contribute to the collimated source function. These two components combine to determine the overall collimated source function. The diffuse source function is defined by scattering from numerous gold nanoshells in the medium reflected, refracted, and diffracted in all directions with the exception of those that point in the collimated direction. The scattered light due to both specular and diffuse reflections points in random and changing directions every time the light hits a nanoshell. The sum of the collimated and diffuse source functions, at any location in the medium pointing in the arbitrary direction $\hat{\mathbf{s}}$, acts as the total source function, which describes the overall intensity and direction of diffuse rays within the nanoshell-embedded medium. Therefore, the total source function can be equated to the diffuse radiative transfer equation, i.e. the left hand side of Eq. (1):

$$\mu\frac{dI_{d\lambda}(\tau_\lambda,\hat{\mathbf{s}})}{d\tau_\lambda} + I_{d\lambda}(\tau_\lambda,\hat{\mathbf{s}}) = S(\tau_\lambda,\hat{\mathbf{s}}) = S_c(\tau_\lambda,\hat{\mathbf{s}}) + S_d(\tau_\lambda,\hat{\mathbf{s}}) \tag{8}$$

where

$$S_c(\tau_\lambda,\hat{\mathbf{s}}) = \frac{\omega_\lambda}{4\pi}\int_{4\pi} I_{c\lambda}(\tau_\lambda,\hat{\mathbf{s}})d\Omega \tag{9}$$

$$S_d(\tau_\lambda,\hat{\mathbf{s}}) = \frac{\omega_\lambda}{4\pi}\int_{4\pi} I_{d\lambda}(\tau_\lambda,\hat{\mathbf{s}})d\Omega \tag{10}$$

Employing the P_1 approximation, the diffuse intensity of radiation can be expressed as

$$I_{d\lambda}(\tau_\lambda,\hat{\mathbf{s}}) \cong \frac{1}{4\pi}(G_{d\lambda} + 3q''_{d\lambda}\mu) \tag{11}$$

The complete derivation of the P_1 approximation is available in Ref. [23].

In order for Eq. (1) to be true, the collimated radiative transfer equation should obey:

$$\mu\frac{dI_{c\lambda}(\tau_\lambda,\hat{\mathbf{s}})}{d\tau_\lambda} + I_{c\lambda}(\tau_\lambda,\hat{\mathbf{s}}) = 0 \tag{12}$$

By applying the following boundary condition to the collimated radiative transfer equation

$$I_{c\lambda}(0,\hat{\mathbf{s}}) = I_{in,\lambda}(0^+,\hat{\mathbf{s}}) \tag{13}$$

As described, the collimated intensity of radiation can be expressed as

$$I_{c\lambda}(\tau_\lambda,\hat{\mathbf{s}}) = I_{in,\lambda}(0^+,\hat{\mathbf{s}})e^{-\tau_\lambda/\mu_c} \tag{14}$$

After substituting $I_{in,\lambda}(0^+,\hat{\mathbf{s}})$ from Eq. (6), the collimated intensity of radiation becomes:

$$I_{c\lambda}(\tau_\lambda,\hat{\mathbf{s}}) = (1-\rho_\lambda(0))q''_{in,\lambda}e^{-\tau_\lambda/\mu_c}\delta(\hat{\mathbf{s}}-\hat{\mathbf{s}}_c) \tag{15}$$

The collimated intensity only includes those rays pointing in the collimated direction $\hat{\mathbf{s}}_c$. Therefore, the dirac-delta function is employed in Eq. (15) to filter out those contributions pointing in directions other than $\hat{\mathbf{s}}_c$. Therefore, only when $\hat{\mathbf{s}} = \hat{\mathbf{s}}_c$ does the collimated intensity of radiation equal to $(1-\rho_\lambda(0))q''_{in,\lambda}e^{-\tau_\lambda/\mu_c}$, otherwise it is zero. In this manner, the collimated fraction of diffuse radiation originating from light scattered by the nanoshells in all directions $\hat{\mathbf{s}}$ is incorporated into the collimated source function. Integrating the collimated intensity of radiation over a 4π solid angle leads to the collimated irradiance, $G_{c\lambda}$, and the collimated radiative heat flux, $q''_{c\lambda}(\hat{\mathbf{s}})$, by following their definitions:

$$G_{c\lambda}(\tau_\lambda) = \int_{4\pi} I_{c\lambda}(\tau_\lambda,\hat{\mathbf{s}})d\Omega = (1-\rho_\lambda(0))q''_{in,\lambda}e^{-\tau_\lambda/\mu_c} \tag{16}$$

$$q''_{c\lambda}(\tau_\lambda,\hat{\mathbf{s}}) = \int_{4\pi} I_{c\lambda}(\tau_\lambda,\hat{\mathbf{s}})\hat{\mathbf{s}}d\Omega = (1-\rho_\lambda(0))q''_{in,\lambda}e^{-\tau_\lambda/\mu_c}\hat{\mathbf{s}}_c \tag{17}$$

The collimated irradiance is independent of direction, while the collimated radiative heat flux is directionally dependent towards $\hat{\mathbf{s}}_c$. When the collimated radiative heat flux is translated to the $\hat{\mathbf{k}}$ direction, the Eq. (17) becomes:

$$q''_{c\lambda}\cos\theta_c(\tau_\lambda,\hat{\mathbf{k}}) = (1-\rho_\lambda(0))q''_{in,\lambda}\left|\hat{\mathbf{s}}_c\cdot\hat{\mathbf{k}}\right|e^{-\tau_\lambda/\mu_c} \tag{18}$$

Similarly for the diffuse part, replacing $I_{d\lambda}$ in Eq. (11), the diffuse radiative transfer Eq. (8) leads to the divergence of radiative heat flux and divergence of irradiance, respectively:

$$\frac{dq''_{d\lambda}}{d\tau_\lambda} = -(1-\omega_\lambda)G_{d\lambda} + \omega_\lambda G_{c\lambda} \tag{19}$$

$$\frac{dG_{d\lambda}}{d\tau_\lambda} = -3q''_{d\lambda} \tag{20}$$

For the P_1 approximation, the two boundary conditions to the diffuse radiative transfer equation are [23]:

$$\tau_\lambda = 0 : q''_d(0,\hat{\mathbf{s}})\cos\theta_c = \int_{4\pi} I_{d\lambda}(0,\hat{\mathbf{s}})\hat{\mathbf{s}}\cdot\hat{\mathbf{k}}\,d\Omega \tag{21}$$

$$\tau_\lambda = \tau_{L\lambda} : q''_d(\tau_{L\lambda},\hat{\mathbf{s}})\cos\theta_c = \int_{4\pi} I_{d\lambda}(\tau_{L\lambda},\hat{\mathbf{s}})\hat{\mathbf{s}}\cdot\hat{\mathbf{k}}\,d\Omega \tag{22}$$

The solutions to both the diffuse radiative heat flux and the diffuse irradiance are, respectively:

$$q''_{d\lambda}\left(\tau_\lambda,\hat{\mathbf{k}}\right) = C_1 e^{\xi_1\tau_\lambda} + C_2 e^{-\xi_1\tau_\lambda} + B_1 e^{-\tau_\lambda/\mu_c} \tag{23}$$

$$G_{d\lambda}(\tau_\lambda) = -\frac{1}{(1-\omega_\lambda)}\left[C_1\xi_1 e^{\xi_1\tau_\lambda} - C_2\xi_1 e^{-\xi_1\tau_\lambda} - \frac{B_1}{\mu_c}e^{-\tau_\lambda/\mu_c} - \omega_\lambda G_{c\lambda}\right] \tag{24}$$

where C_1 and C_2 are analytical constants obtained by solving:

$$\begin{bmatrix} C_1 \\ C_2 \end{bmatrix} = \begin{bmatrix} B_2 & B_3 \\ B_6 & B_7 \end{bmatrix}^{-1}\begin{bmatrix} B_4B_1 + B_5 \\ B_8B_1 + B_9 \end{bmatrix} \tag{25}$$

The B's and ξ_1 constants are tabulated in Table 1.

The term ε_λ appearing in Table 1 defines the proportion of the incoming light that is transmitted through the boundary surface. It is equal to $(1-\rho_\lambda(0))$ at the entry boundary or $(1-\rho_\lambda(\tau_{L\lambda}))$ at the exit boundary. $H_{c0,\lambda}$ and $H_{cL,\lambda}$ are the shorter terms for $H_{c\lambda}$ at locations $\tau_\lambda = 0$ and $\tau_\lambda = \tau_{L\lambda}$, respectively. These terms represent the sum of incoming collimated rays augmented at the corresponding boundaries by multiple internal reflections of the collimated radiation by both boundaries. $H_{c0,\lambda}$ and $H_{cL,\lambda}$ are respectively described as follows:

$$H_{c\lambda}(0) = H_{c0,\lambda} = G_{c\lambda}[\rho(\tau_L)e^{-\tau_{L\lambda}/\mu_c} + \rho_\lambda(0)\rho_\lambda^2(\tau_L)e^{-3\tau_{L\lambda}/\mu_c} + \cdots] \tag{26}$$

$$H_{c\lambda}(\tau_{L\lambda}) = H_{cL,\lambda} = G_{c\lambda}[1 + \rho_\lambda(0)\rho_\lambda(\tau_L)e^{-2\tau_{L\lambda}/\mu_c} + \cdots] \tag{27}$$

In this study, the mismatch of refractive indices between the surrounding air and the host slab material is minimal, and as a result, reflections at the boundary are relatively insignificant, ρ_λ is very small, and in the model, all the ρ_λ terms disappear. Thus, good accuracy is obtained by completely disregarding the reflected collimated radiation, or in other words, taking $H_{c0,\lambda}$ and $H_{cL,\lambda}$ to be 0 and $G_{c\lambda}$, respectively. The host slab medium is considered transparent to incoming radiation due to a small optical thickness, which is a factor of both the extinction properties of the medium and the physical length the radiation travels along the depth.

Table 2
Nondimensional parameters for radiative heat flux and irradiance

Radiative heat flux		Irradiance	
Symbol	Definition	Symbol	Definition
$\Psi_{d\lambda}$	$\frac{q''_{d\lambda}}{q''_{in,\lambda}}$	$\Phi_{d\lambda}$	$\frac{G_{d\lambda}}{q''_{in,\lambda}}$
$\Psi_{c\lambda}$	$\frac{q''_{c\lambda}\lvert\hat{\mathbf{s}}_c\cdot\hat{\mathbf{k}}\rvert}{q''_{in,\lambda}}$	$\Phi_{c\lambda}$	$\frac{G_{c\lambda}}{q''_{in,\lambda}}$
$\Psi_{R\lambda}$	$\frac{q''_{d\lambda}+q''_{c\lambda}\lvert\hat{\mathbf{s}}_c\cdot\hat{\mathbf{k}}\rvert}{q''_{in,\lambda}} = \frac{q''_{R\lambda}}{q''_{in,\lambda}}$	$\Phi_{R\lambda}$	$\frac{G_{d\lambda}+G_{c\lambda}}{q''_{in,\lambda}} = \frac{G_{R\lambda}}{q''_{in,\lambda}}$

The total radiative heat flux at any location in the medium pointing towards $\hat{\mathbf{k}}$, obtained by taking an integration of each term in Eq. (7) over a 4π solid angle, is given as

$$q''_{R\lambda}(\tau_\lambda,\hat{\mathbf{k}}) = q''_{d\lambda}(\tau_\lambda,\hat{\mathbf{k}}) + q''_{c\lambda}(\tau_\lambda,\hat{\mathbf{s}})\left|\hat{\mathbf{s}}_c\cdot\hat{\mathbf{k}}\right| \tag{28}$$

After taking the derivative of the collimated radiative heat flux from Eq. (18) and summing that with the divergence of the diffuse radiative heat flux, Eq. (19), the divergence of the total radiative heat flux can be given as

$$\frac{dq''_{R\lambda}(\tau_\lambda)}{d\tau_\lambda} = -(1-\omega_\lambda)G_{R\lambda}(\tau_\lambda) \tag{29}$$

where the total irradiance, $G_{R\lambda}$, is obtained by integrating each term in Eq. (7) over 4π in accordance with its definition:

$$G_{R\lambda}(\tau_\lambda) = G_{d\lambda}(\tau_\lambda) + G_{c\lambda}(\tau_\lambda) \tag{30}$$

The nondimensionalized parameters for both radiative heat flux and irradiance are presented in Table 2.

3. Heat generation and temperature distribution

As light is absorbed, heat is generated by the nanoshells and released into the medium. Both boundary surfaces are subjected to convection for the purpose of future experimental validation. Seven assumptions were made to solving the temperature distribution due to heat generation: (1)

Table 1
Analytical constants

B_1	$-\frac{1}{\mu_c}\frac{\omega_\lambda(1-\rho_\lambda(0))q''_{in,\lambda}}{\frac{1}{\mu_c}-\xi_1^2}$	B_2	$2-\frac{\varepsilon_\lambda}{(2-\varepsilon_\lambda)(1-\omega_\lambda)}\xi_1$
B_3	$2+\frac{\varepsilon_\lambda}{(2-\varepsilon_\lambda)(1-\omega_\lambda)}\xi_1$	B_4	$-\left(2+\frac{\varepsilon_\lambda}{(2-\varepsilon_\lambda)(1-\omega_\lambda)}\frac{1}{\mu_c}\right)$
B_5	$-\frac{\varepsilon_\lambda}{2-\varepsilon_\lambda}\frac{\omega_\lambda}{1-\omega_\lambda}(1-\rho_\lambda(0))q''_{in,\lambda}+\frac{4(1-\varepsilon_\lambda)}{2-\varepsilon_\lambda}H_{c0,\lambda}$	B_6	$-\left(2e^{\xi_1\tau_{L\lambda}}+\frac{\varepsilon_\lambda}{(2-\varepsilon_\lambda)(1-\omega_\lambda)}\xi_1 e^{\xi_1\tau_{L\lambda}}\right)$
B_7	$-2e^{-\xi_1\tau_{L\lambda}}+\frac{\varepsilon_\lambda}{(2-\varepsilon_\lambda)(1-\omega_\lambda)}\xi_1 e^{-\xi_1\tau_{L\lambda}}$	B_8	$2e^{-\tau_{L\lambda}/\mu_c}-\frac{\varepsilon_\lambda}{(2-\varepsilon_\lambda)(1-\omega_\lambda)}\frac{e^{-\tau_{L\lambda}/\mu_c}}{\mu_c}$
B_9	$-\frac{\varepsilon_\lambda}{2-\varepsilon_\lambda}\frac{\omega_\lambda}{1-\omega_\lambda}(1-\rho_\lambda(0))q''_{in,\lambda}e^{-\tau_{L\lambda}/\mu_c}+\frac{4(1-\varepsilon_\lambda)}{2-\varepsilon_\lambda}H_{cL,\lambda}$	ξ_1	$\sqrt{3(1-\omega_\lambda)}$

The physical and thermal properties of the host medium are constant, (2) the nanoshells contribute negligible additional effects to the physical and thermal properties of the medium, (3) the medium is homogeneous, (4) the convective terms are constant over time, (5) the medium is one-dimensional, (6) emission is negligible, and (7) the host medium is transparent to spectral irradiation. The energy equation incorporating these assumptions can be expressed as [23]:

$$\frac{1}{\alpha_{md}}\frac{dT}{dt} = \frac{d^2T}{dz^2} + \frac{u'''}{k_{md}} \tag{31}$$

where u''' is the local heat generation spectrum across the depth of the medium created by gold nanoshells. It is defined as the negative sign of the divergence of radiative heat flux.

$$u''' = -\frac{dq''_{R\lambda}}{dz} \tag{32}$$

The normalized heat generation term, U^*, defines the ratio of division of heat generation term, u''', and the spectral extinction coefficient, β_λ, to the spectral input radiation.

$$U^* = \frac{u'''/\beta_\lambda}{q''_{in,\lambda}} \tag{33}$$

The temperature distribution for transient time is solved using the finite difference explicit method [24,25]. The energy equation is discretized in time and space and the stability criterion is applied. An additional assumption taken to the finite difference solving method is that the temperature of the nanoshells and the surrounding medium up to half of the clearance distance between the spatial nodes in the depth direction is the same.

4. Results and discussion

4.1. Radiative heat transfer analysis

In this study, a sample calculation is made by incorporating the optical properties of gold nanoshells reported experimentally in [9]. The slab material in which these nanoshells are uniformly distributed is 3 cm-thick polydimethylsiloxane (PDMS). A uniformly distributed light is directed normal to the face of the slab at a wavelength of 820 nm. The thickness of the slab is assumed to be much smaller than its side dimensions to allow one-dimensional analysis with negligible errors due to multidimensionality. The properties of PDMS are taken as [26]: $\rho = 965$ kg/m^3, $c = 1460$ J/kg K, $k = 0.17$ W/m K, and $n = 1.49$.

With the 820-nm incident radiation situated between 650- and 1000-nm wavelengths, two different types of gold nanoshells are employed; one has an absorptive optical configuration and the other has a scattering optical configuration. The absorptive optical configuration has an absorption that contributes a larger fraction to extinction than scattering, while the scattering optical configuration means the opposite. Utilized optical properties of both types of gold nanoshells are presented in Fig. 2. Experimental absorption and scattering efficiency values from the selected literature lie within ±0.05 from the utilized absorption and scattering efficiency values used in this study. Experimental extinction efficiency values lie within ±0.1 from the utilized extinction efficiency values. Optimum extinction for both configurations is located between 800- and 850-nm wavelengths.

At the 820-nm wavelength, the scattering albedo for the absorptive and scattering configuration is 0.286 and 0.881, respectively. The boundary reflection is minimal as the calculated reflectivity value is found to be 0.04. The mismatch of refractive index has contributed very little drop in the radiative heat flux as compared to that without any mismatch of refractive index.

The collimated and diffuse radiative heat fluxes are shown in Fig. 3 for both absorptive and scattering configurations for different optical lengths. Quantitatively, the nanoshell concentrations needed to produce optical lengths of 0.1, 1, and 10 are approximately 7.0174×10^{13}, 7.0174×10^{14}, and 7.0174×10^{15} particles per cubic meter. As mentioned, the collimated radiative heat flux decays exponentially due to attenuation by gold nanoshells. As the optical length is taken into a higher order of magnitude, the extinction coefficient increases by the same order of magnitude leading to a larger decay in collimated radiative heat flux. Variation in scattering albedo does not change the collimated radiative decay because the decay in collimated radiation only sees the total extinction. However, scattering is an important parameter for the diffuse radiative heat flux because scattering helps distribute radiation more evenly. Under the absorptive configuration, diffuse radiative heat flux does not give a significant contribution to the total radiative heat flux. It is the reason why the total radiative heat flux spectrum experiences minimal alteration from the collimated radiative heat flux spectrum when scattering is low, as shown in Fig. 4. On the other hand, under the scattering configuration, diffuse radiative heat flux gives

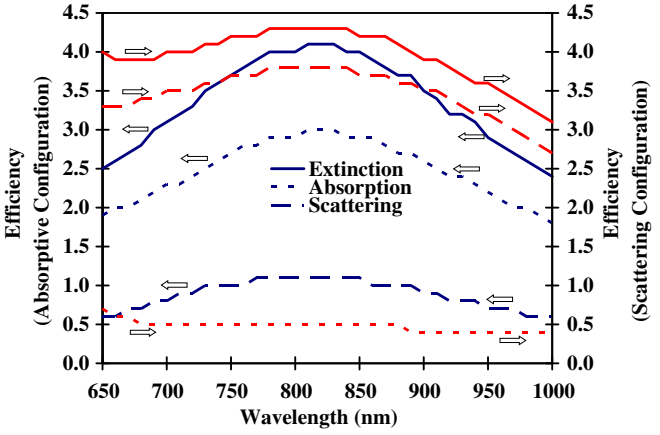

Fig. 2. Optical properties of gold nanoshells in absorptive configuration and scattering configuration; reproduced from [9].

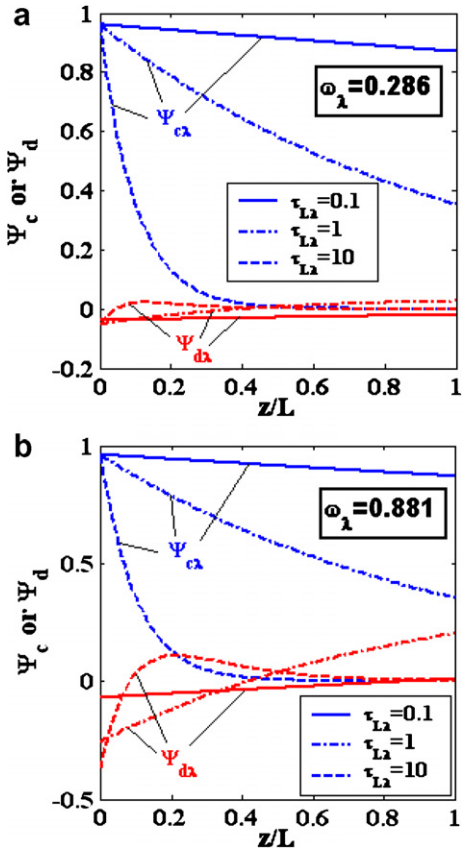

Fig. 3. Normalized collimated and diffuse radiative heat flux. (a) Absorption; (b) scattering.

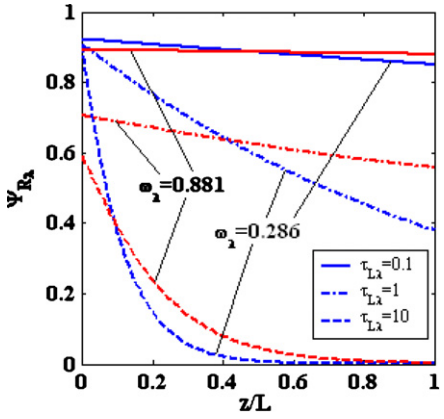

Fig. 4. Influence of optical length to radiative heat flux decay.

significant contribution to the total radiative heat flux creating a more even radiative distribution. This is shown through the significant alteration of total radiative heat flux decay from the collimated radiative heat flux decay. It is also clearly shown in Fig. 4 that the radiative decay under the scattering configuration is more even than the radiative decay under the absorptive configuration.

Small extinction spreads the radiation more evenly across the medium compared to large extinction; however, small extinction also corresponds to low energy absorption to generate heat. As the optical length increases, more radiation is attenuated due to absorption and scattering per unit depth. For a reasonably large optical length ($\tau_{L\lambda} \gg 1$), one should expect a negligible amount of radiation by the nanoshells in the rear region or even some portion in the entry region for a very large optical length due to the large amount of attenuation for each unit depth the light travels.

Holding the same extinction coefficient at $\tau_{L\lambda} = 1$, the influence of variation in scattering albedo to the total radiative decay is given in Fig. 5. It is apparent that the scattering configuration of nanoshells results in a much more flat radiative heat flux curve than the absorptive configuration under the same extinction. Scattering improves the diffuse radiation creating a more even radiative distribution. The total radiation under the absorptive configuration diminishes closer to the entry boundary more significantly than that under the scattering configuration, proving scattering promotes a more uniform radiative distribution along the depth. With the absence of diffuse scattering, the diffuse radiation permeating the medium, creating a diffuse "essence" throughout the medium, is also absent, and thus, the total spectral radiative heat flux is the same as the spectral collimated radiative heat flux. In the case of both the absence of scattering and a mismatch of refractive indices, the normalized radiative heat flux starts at 1 at the entry boundary ($z/L = 0$) and decays in the amount of $e^{-\kappa_\lambda z/\mu_c}$ at any depth location.

4.2. Heat generation and temperature distribution

The influence of the optical length and the scattering albedo to heat generation and temperature distribution is analyzed. Both boundaries are subjected to convection with convective coefficient, h, of 10 W/m^2 K and environment temperature, T_∞, at 27 °C. The input power is taken as 300 kW/m^2. This nominal value of input power is reasonably chosen after having learned the utilized values for input power from several sources in the literature: 0.008 W/m^2 [8], 20–60 kW/m^2 [10], 440 kW/m^2 [7], and 200–880 kW/m^2 [14]. Fig. 6 shows the heat generation/heat

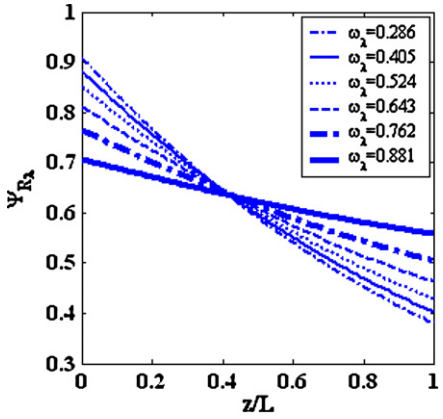

Fig. 5. Influence of scattering albedo to radiative heat flux decay ($\tau_{L\lambda} = 1$).

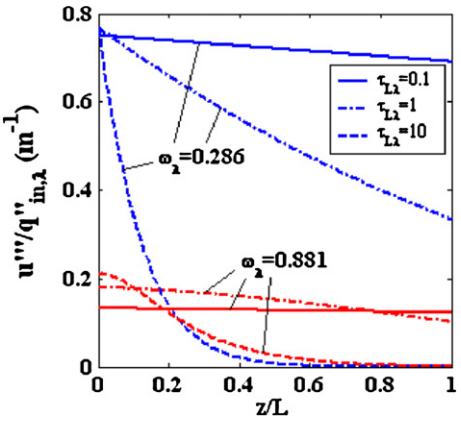

Fig. 6. Influence of optical length to heat generation within the medium.

flux ratio, $u'''/q''_{\text{in},\lambda}$, which is obtained by multiplying the normalized heat generation with the extinction coefficient. Along with depth location, the heat generation does not decay much with $\tau_{L\lambda} = 0.1$. For $\tau_{L\lambda} = 10$, because of the rapid decay, the heat generation is very high in the entry region and significantly lower in the rear region. Because a large amount of radiation is absorbed per unit length, a negligible amount penetrates into the rear region. Therefore, a significantly larger amount of heat is generated in the entry region than in the rear region.

Heat generation is also influenced by the scattering albedo. Fig. 7 shows transitional trends of heat generation between the absorptive configuration and scattering configuration with $\tau_{L\lambda} = 1$. Holding the same extinction, more radiation is absorbed per unit length for the absorptive configuration than for the scattering configuration, because the magnitude of heat generation is dependent on the magnitude of absorption. Thus, for a small optical length, a larger scattering albedo produces a smaller magnitude, but a more even distribution of heat generation than that for the case of the smaller scattering albedo. However, for a large optical length, the magnitude in the rear region is in fact smaller for the absorptive configuration. This occurs, again, because most of the radiation has been absorbed in the entry region, and the radiation in the rear region becomes negligible. When radiation is minimal, nanoshells have minimal energy to produce heat.

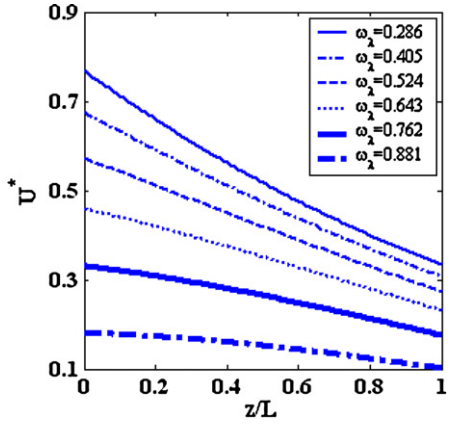

Fig. 7. Influence of scattering albedo to heat generation ($\tau_{L\lambda} = 1$).

The following observation on temperature distribution, presented in Fig. 8, is based on the heat generation analysis. The finite difference simulation begins with all nodal initial temperatures at the environment temperature, T_∞, and ends when the temperature of the entry boundary reaches 200 °C. In other words, the stopping criterion is when the temperature increase at the entry boundary is 173 °C. The temperature distribution under this stopping criterion does not exceed the melting temperature of PDMS. The average inter-nanoshell clearance for selected particle concentrations is in the μm scale. Initially, the slab was discretized in the order of 10^4 nodes in order to be in the same scale as the inter-nanoshell clearance, but, in fact, the size of discretized space is actually two orders of magnitudes higher than the scale of spacing. Under this grid size, numerical convergence is achieved.

An increase in the optical length corresponds to an increase in the extinction coefficient because the length of the medium does not change. At a small optical length, a near parabolic temperature distribution is achieved because the heat generation is nearly constant across the depth of the medium. As the extinction increases, the top deflection point moves towards the entry boundary because the absorption per unit length increases. This means that more heat from nanoshells is dissipated closer to the entry boundary along with the increase in optical length. This phenomenon is clearly presented in the temperature distribution at $\tau_{L\lambda} = 10$. A mimic of exponential decay occurs approximately in the region $0.3 < z/L < 1$ for the scattering configuration or $0.1 < z/L < 1$ for the absorptive configuration showing a significant contribution of transient conduction. When more energy is absorbed in the entry region, the temperature of the hot portion in the entry region increases rapidly. Since the radiation magnitude decreases significantly in the rear region, conduction becomes a significant mode of heat transfer due to temperature difference between the entry and rear regions.

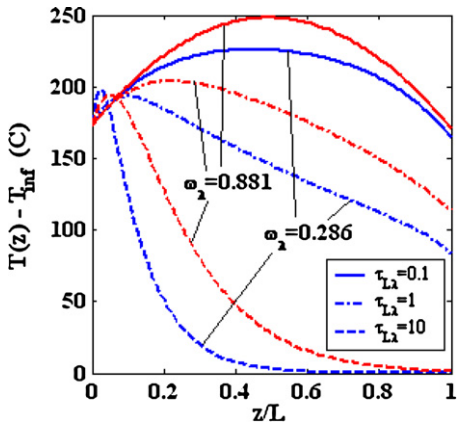

Fig. 8. Influence of optical length to the temperature distribution when temperature rise at boundary $z/L = 0$ reaches 173 °C; numerical time for each temperature distribution is presented in Fig. 9.

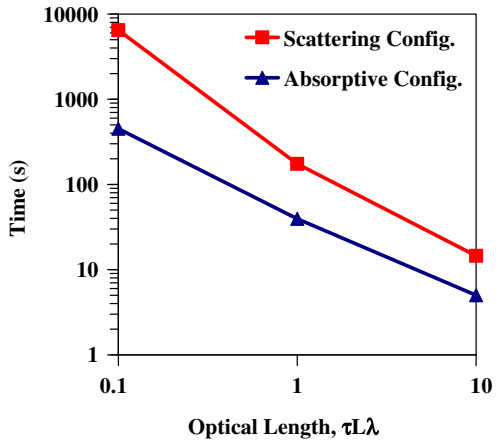

Fig. 9. Numerical time for $\tau_{L\lambda} = 0.1$, 1, and 10.

The required numerical time drops as optical length is increased as shown in Fig. 9. One may recall that the numerical stopping criterion is when the increase in temperature at the entry boundary reaches 173 °C. For the absorptive configuration, the required numerical times for optical lengths of 0.1, 1, and 10 are 451.25, 39.5, 5 s, respectively; while for the scattering configuration, these numbers are 6479, 174, and 14.5 s, respectively. As optical length is increased, more radiation is absorbed for each unit depth that the light travels. For the case of $\tau_{L\lambda} = 10$, because most of the radiation is absorbed significantly in the front portion of the entry region and because the heat generation peaks near the entry boundary, the entry boundary temperature increases at an extremely high rate. As shown in Fig. 8, the temperature in the rear region has not even fully received the heat by conduction at the stopping time. While, for the case of $\tau_{L\lambda} = 0.1$, radiation spreads out along the depth. Therefore, the heat generation is more effectively distributed across the whole volume of slab; therefore, it takes a significantly longer time for the entry boundary to reach the stopping temperature than that of $\tau_{L\lambda} = 10$.

The temperature distribution of the scattering configuration is relatively higher than that of the absorptive configuration due to the smaller absorption coefficient as shown in Fig. 10. Despite having the same total attenuation, the

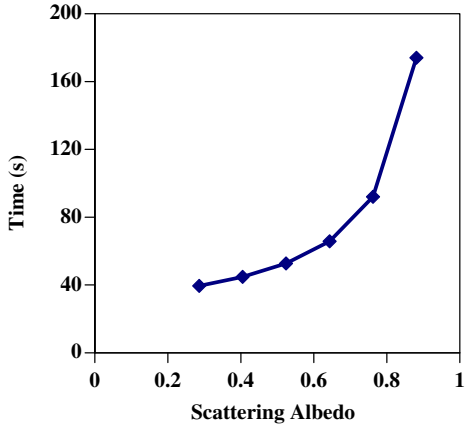

Fig. 10. Numerical time of variation in scattering albedo for $\tau_{L\lambda} = 1$.

absorptive configuration should have a shorter numerical time than the scattering configuration. Because of the absorptive configuration, more radiation is absorbed per unit length, and as a result, more heat is generated per unit length. Moreover, less radiation is distributed into the depth due to the small amount of scattering. On the other hand, for the scattering configuration, a smaller amount of heat is dissipated by the nanoshells per unit length, and more radiation is distributed into the depth. Therefore, the entry boundary temperature should reach the stopping condition slower for the scattering configuration than for the absorptive configuration.

4.3. Justification for neglecting emission

In this study, the emission contribution to the radiative heat flux is neglected. However, since everything that has a temperature emits, the emission magnitude is observed as if its inclusion in the radiative transfer equation would not give a significant effect. If emission is considered, the equation of divergence of radiative heat flux, Eq. (29), becomes:

$$\frac{\mathrm{d}q''_{\mathrm{R}\lambda}(\tau_\lambda)}{\mathrm{d}\tau_\lambda} = (1-\omega_\lambda)[4\pi I_{\mathrm{b}\lambda}(\tau_\lambda) - G_{\mathrm{R}\lambda}(\tau_\lambda)] \tag{34}$$

where $I_{\mathrm{b}\lambda}$ is the spectral blackbody intensity of radiation. The blackbody emissive power, E_{b}, which contains the temperature term, is equal to the integral of the spectral blackbody emissive power over all possible wavelengths.

$$E_{\mathrm{b}} = \sigma T^4 = \frac{1}{\pi}\int_0^\infty I_{\mathrm{b}\lambda}\mathrm{d}\lambda \tag{35}$$

The gray input radiation is obtained by integrating the spectral input radiation over all possible wavelengths.

$$q''_{\mathrm{in}} = \int_0^\infty q''_{\mathrm{in},\lambda}\mathrm{d}\lambda \tag{36}$$

However, since the spectral input radiation comes in one wavelength, the magnitude of gray input radiation is the same as that of spectral input radiation. The justification in assuming negligible emission is made by comparing the relative magnitude of normalized emission term, Φ_{b}, with the normalized irradiance, $\Phi_{\mathrm{R}\lambda}$, at any location τ_λ. The normalized emission term is defined as

$$\Phi_{\mathrm{b}}(\tau_\lambda) = \frac{4\sigma T^4(\tau_\lambda)}{q''_{\mathrm{in}}} \tag{37}$$

Fig. 11 shows the effect of optical length variation to the irradiance of the absorptive configuration. An increasing optical length produces larger irradiance decay. The utilized temperature values are those presented at $\tau_{L\lambda} = 1$ in Fig. 8 given the surrounding temperature, T_∞, at 27 °C. It is apparent that an increase in scattering albedo at the same optical length results in a decrease in the Φ_{b}-to-$\Phi_{\mathrm{R}\lambda}$ ratio. Because an increase in scattering causes the diffuse irradiance to rise, the total irradiance rises as well. In

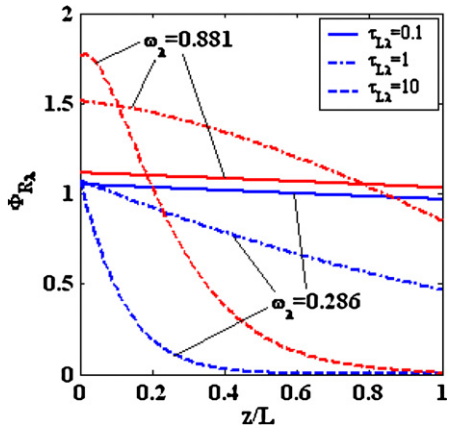

Fig. 11. Influence of optical length to irradiance.

addition, the increase in irradiance due to scattering albedo variation is relatively higher than the increase in temperature distribution at the stopping condition.

Fig. 12 shows the ratio of the blackbody emission term to the spectral irradiance for a series of scattering albedo values at $\tau_{L\lambda} = 1$. Values of the Φ_b-to-$\Phi_{R\lambda}$ ratio are all under 5%, showing that neglecting emission is justified. In the case of temperature, the effect by emission becomes more significant if the stopping criterion is at higher temperatures because emissive power is a function of T^4. The limit to the stopping criterion will surely be such that the temperature distribution does not exceed the melting temperature of the medium.

Lastly, for smaller optical lengths, lower values of Φ_b-to-$\Phi_{R\lambda}$ ratio are expected at all locations. However, when a large optical length ($\tau_{L\lambda} \gg 1$) is considered, most of the radiation is attenuated in the entry region leaving a negligible amount of radiation in the rear region as explained earlier. This has caused the temperature augmentation due to radiation to be significant in the entry region but minimal in the rear region. Thus, for a very large optical length, the Φ_b-to-$\Phi_{R\lambda}$ ratio is not the best representation to observe the relative magnitude of the emission term and the irradiance term, especially in the rear region.

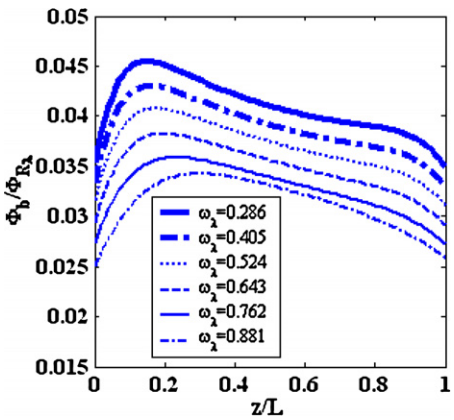

Fig. 12. Proportion of the emission term to the irradiance ($\tau_{L\lambda} = 1$).

The significant difference in the rate of temperature increase between the entry and rear regions makes the heat from higher temperature portion (some portion in the entry region) to flow to the lower temperature portion (rear region). Thus, it is obvious that conduction contributes larger to the temperature increase of nanoshells in the rear region than radiation does. Contribution of emission by nanoshells to the medium is essentially demonstrated through the radiative exchange between nanoshells at different temperatures within the transparent wavelength range of the medium. This happens at a relatively high temperature where emissive power has become comparable to conduction. In the lower temperature region, nanoshells add their rate of temperature increase by receiving radiation from those in the higher temperature region in addition to conduction. Neglecting the influence of the thermal conductivity of the gold nanoshells, this phenomenon shows that, at relatively high temperatures, the heat transfer within the medium can be increased due to inter-nanoshell radiative exchange.

5. Conclusion

The heating of a one-dimensional, conducting and radiatively participating medium due to embedded absorbing and scattering nanoparticles is solved. Variation of the concentration and the configuration of gold nanoshells is found to cause an alteration in the radiative transfer spectrum, which leads to an alteration in the local heat generation spectrum and the resulting temperature distribution. Proper nanoshell concentration should be selected in order to obtain the desired magnitude of radiative decay because this determines the resulting decay of the local heat generation spectrum. A nanoshell configuration with a great amount of scattering increases the internal diffuse radiation, creating a more even radiative distribution to the total radiation spectrum from collimated radiation. The temperature distribution at the stoppage condition has been obtained in the case where both boundaries are subjected to convection.

The situation posed in this problem using PDMS as the host medium can be experimentally verified and used to generate a model for the dynamics of nanoshell heating in human tissue. In this study, PDMS is considered fully transparent to the collimated radiation, because it is nearly fully transparent with its low extinction under the wavelength used and the depth penetrated. In tissue modeling, the near-infrared regime also presents a nearly fully transparent situation, and wavelengths between 600 and 1400 nm comprise what is called the "therapeutic window". Since the optical resonance of gold nanoshells can be "tuned" by changing the relative dimensions of core diameter and shell thickness, gold nanoshells can be manufactured to absorb or scatter within the therapeutic window. A direct application for this research is the photothermal therapy of tumors. By absorbing light at a near-infrared wavelength, a cluster of gold nanoshells is capable of

annihilating a tumor cell by heating it up beyond its damage threshold temperature [6–8,10,11]. Other possible applications include blood immunoassay [3–5], noninvasive tissue imaging [8,12,13], and laser tissue soldering [14].

The modeling of PDMS provides the framework for research in such radiative heat transfer applications. Incorporating absorption into the PDMS model and comparing with experiment will allow for more realistic tissue modeling which, even within the therapeutic window, calls for absorption and scattering of various degrees by various depths of skin, muscle, and bone – before even reaching the absorbing nanoshell embedded medium. Future studies shall call for such multi-layered and multi-absorbant/scattering analysis to provide more realistic models for nanoshells used in biomedical applications or any other application utilizing a participating host material.

Acknowledgements

The seminar series of the Laboratory of Nanophotonics (LANP) at Rice University, and proofreading efforts by Jerry Vera are acknowledged.

References

[1] S.J. Oldenberg, R.D. Averitt, S.L. Westcott, N.J. Halas, Nanoengineering of optical resonances, Chem. Phys. Lett. 28 (1998) 243–247.
[3] L.R. Hirsch, J.L. West, J.B. Jackson, A. Lee, N.J. Halas, A rapid, whole blood immunoassay using metal nanoshells, in: Proceedings of the 25th Annual International Conference of the IEEE EMBS, Cancun, Mexico, September 17–21, 2003, pp. 3442–3443.
[4] L.R. Hirsch, J.B. Jackson, A. Lee, N.J. Halas, J.L. West, A whole blood immunoassay using gold nanoshells, Anal. Chem. 75 (10) (2003) 2377–2381.
[5] L.R. Hirsch, N.J. Halas, J.L. West, A rapid, near infrared, whole blood immunoassay using metal nanoshells, in: Proceedings of the Second Joint EMBS/BMES Conference, Houston, Texas, October 23–26, 2002, pp. 1646–1647.
[6] L.R. Hirsch, R.J. Stafford, J.A. Bankson, S.R. Sershen, R.E. Price, J.D. Hazle, N.J. Halas, J.L. West, Targeted photothermal tumor therapy using metal nanoshells, in: Proceedings of the Second Joint EMBS/BMES Conference, Houston, Texas, October 23–26, 2002, pp. 530–531.
[7] L.R. Hirsch, J.L. West, R.J. Stafford, J.A. Bankson, S.R. Sershen, R.E. Price, J.D. Hazle, N.J. Halas, Nanoshell-mediated near infrared photothermal tumor therapy, in: Proceedings of the 25th Annual International Conference of the IEEE EMBS, Cancun, Mexico, September 17–21, 2003, pp. 1230–1231.
[8] C. Loo, A. Lowery, N. Halas, J. West, R. Drezek, Immunotargeted nanoshells for integrated cancer imaging and therapy, Nano Lett. 5 (4) (2005) 709–711.
[9] A.W.H. Lin, C.H. Loo, L.R. Hirsch, J.K. Barton, M.-H. Lee, N.J. Halas, J.L. West, R.A. Drezek, Nanoshells for integrated diagnosis and therapy of cancer, in: Nanosensing: Materials and Devices, Proc. SPIE 5593 (2004) 308–316.
[10] D.P. O'Neal, L.R. Hirsch, N.J. Halas, J.D. Payne, J.L. West, Photothermal cancer therapy using intravenously injected near infrared-absorbing nanoparticles, in: Optical Methods for Tumor Treatment and Detection: Mechanisms and Techniques in Photodynamic Therapy XIV, Proc. SPIE 5689 (2005) 149–157.
[11] D.P. O'Neal, L.R. Hirsch, N.J. Halas, J.D. Payne, J.L. West, Photothermal tumor ablation in mice using near infrared-absorbing nanoparticles, Cancer Lett. 209 (2004) 171–176.
[12] C. Loo, L. Hirsch, M.-H. Lee, E. Chang, J. West, N. Halas, R. Drezek, Gold nanoshell bioconjugates for molecular imaging in living cells, Opt. Lett. 30 (9) (2005) 1–3.
[13] J.K. Barton, N.J. Halas, J.L. West, R.A. Drezek, Nanoshells as an optical coherence tomography contrast agent, in: Coherence Domain Optical Methods and Optical Coherence Tomography in Biomedicine VIII, Proc. SPIE 5316 (2004) 99–106.
[14] A.M. Gobin, D.P. O'Neal, N.J. Halas, R.A. Drezek, J.L. West, Laser tissue soldering with near-infrared absorbing nanoparticles, Proc. SPIE 5686 (2005) 261–266.
[17] C. Oubre, P. Nordlander, Optical properties of metallodielectric nanostructures calculated using the finite difference time domain method, J. Phys. Chem. B 108 (2004) 17740–17747.
[18] P.D. Jones, Y. Bayazitoglu, Radiative enchancement of heat transfer to a gray gas through particle seeding, Numer. Heat Transfer, Part A 27 (6) (1995) 665–680.
[19] C.C. Tseng, R. Viskanta, Heating/melting of a semitransparent particle including radiation effects, Int. J. Therm. Sci. 40 (10) (2006) 945–954.
[20] A. Wang, M.F. Modest, Monte carlo schemes for radiative transfer in media represented by particle fields, in: Proceedings of IMECE2005, Orlando, Florida, USA, November 5–11, 2005.
[21] S.R. Sershen, S.L. Westcott, J.L. West, N.J. Halas, An opto-mechanical nanoshell-polymer composite, Appl. Phys. B: Lasers Opt. 73 (2001) 379–381.
[22] S.R. Sershen, S.L. Westcott, N.J. Halas, J.L. West, Independent optically addressable nanoparticle-polymer optomechanical composites, Appl. Phys. Lett. 80 (24) (2002) 4609–4611.
[23] M. Modest, Radiative Heat Transfer, second ed., Academic Press, 2003.
[24] H.S. Carslaw, J.C. Jaeger, Conduction of Heat in Solids, Oxford University Press, 1986.
[25] S.C. Chapra, R.P. Canale, Numerical Methods for Engineers, fourth ed., McGraw-Hill, 2003.
[26] J.E. Mark, Physical Properties of Polymers Handbook, AIP Press, 1996.